J|A|C|S
ARTICLES
Published on Web 11/08/2007

Helical Polymer $^1/_\infty[P_2Se_6^{2-}]$: Strong Second Harmonic Generation Response and Phase-Change Properties of Its K and Rb Salts

In Chung,[†,‡] Christos D. Malliakas,[†,‡] Joon I. Jang,[§] Christian G. Canlas,[†] David P. Weliky,[†] and Mercouri G. Kanatzidis*[,†,‡]

Contribution from the Department of Chemistry, Michigan State University, East Lansing, Michigan 48864, Department of Chemistry, Northwestern University, Evanston, Illinois 60208, and Department of Physics and Astronomy, Northwestern University, Evanston, Illinois 60208

Received July 10, 2007; E-mail: m-kanatzidis@northwestern.edu

Abstract: The selenophosphates $A_2P_2Se_6$ (A = K, Rb) crystallize in the chiral trigonal space group $P3_121$, with $a = 7.2728(9)$ Å, $c = 18.872(4)$ Å, and $Z = 3$ at 298(2) K and $a = 14.4916(7)$ Å, $c = 18.7999(17)$ Å, and $Z = 12$ at 173(2) K for K^+ salt and $a = 7.2982(5)$ Å, $c = 19.0019(16)$ Å, and $Z = 3$ at 100(2) K for Rb^+ salt. The $A_2P_2Se_6$ feature parallel one-dimensional helical chains of $^1/_\infty[P_2Se_6^{2-}]$ which depict an oxidative polymerization of the ethane-like $[P_2Se_6]^{4-}$ anion. On cooling well below room temperature $K_2P_2Se_6$ exhibits a displacive phase transition to a crystallographic subgroup and forms a superstructure with a cell doubling along the *a*- and *b*-axes. The Rb analogue does not exhibit the phase transition. The compounds are air stable and show reversible glass-crystal phase-change behavior with a band gap red shift of 0.11 and 0.22 eV for K^+ and Rb^+ salts, respectively. Raman spectroscopy, ^{31}P magic angle spinning solid-state NMR, and pair distribution function (PDF) analysis for crystalline and glassy $K_2P_2Se_6$ give further understanding of the phase transition and the local structure of the amorphous state. $K_2P_2Se_6$ exhibits excellent mid-IR transparency and a strong second harmonic generation (SHG) response. The SHG response is type-I phase-matchable and in the wavelength range of 1000−2000 nm was measured to be 50 times larger than that of the commercially used material $AgGaSe_2$. Glassy $K_2P_2Se_6$ also exhibits an SHG response without the application of electric field poling. In connection with the NLO properties the thermal expansion coefficients for $K_2P_2Se_6$ are reported.

1. Introduction

The chalcophosphate anions show great structural diversity and are a predominantly discrete molecular species as for example the $[PSe_4]^{3-}$,[1] $[P_2Se_6]^{4-}$,[2] $[P_2Se_9]^{4-}$,[3] $[P_8Se_{18}]^{6-}$,[4] and the *trans*-decalin-like $[P_6Se_{12}]^{4-}$.[5] The number of infinite anions is very small and includes $^1_\infty[PSe_6^-]$[6] and $^1_\infty[P_5Se_{10}^{5-}]$. The latter is found bonded to transition metal atoms in $A_3MP_5Se_{10}$ (A = K, Rb; M = Ru, Os).[7] The polymeric anions show unusual structural moieties and coordination chemistry compared to the classical $[PSe_4]^{3-}$ and $[P_2Se_6]^{4-}$. All chalcophosphates are potential ligands to metal ions for building finite or extended structures.[8] The anions can be easily stabilized in polychalcogenide fluxes of suitable composition. Our experimental investigations of alkali selenophosphates provided useful insights on the relationship between structure and flux composition (A/P/Se ratio in the composition) in this class.[5] The diversity of these anions seems greater than that of the oxo-phosphate anions which are responsible for defining the enormous class of metal phosphates. The chalcophosphate anions, for example, are capable of condensing via Q−Q bonds, whereas the phosphates are not known to do so. Therefore, the chalcogenide analogues have the potential to produce an even greater family of compounds with metal ions. One striking contrast between phosphates and chalcophosphates is the ability of the latter to couple through Q−Q bonds (Q = S, Se) forming catenated species. In principle, every simple molecular anion $[P_xQ_y]^{z-}$ could be oxidatively coupled through its terminal P−Q bonds to form larger species linked with P−Q−Q−P moieties.

Here we describe the unique helical anion $^1_\infty[P_2Se_6^{2-}]$ in the form of K^+ and Rb^+ salts. Although it was not formed via actual oxidative coupling chemistry, the chiral structure derives from coupling of the ethane-like $[P_2Se_6]^{4-}$ anion. Both $K_2P_2Se_6$ and $Rb_2P_2Se_6$ can be quenched from the melt to a glassy state and can undergo reversible phase-change crystal-glass transitions. Interest in phase-change materials is growing, as a result of emerging technologies including commercially available rewritable optical media and the development of nonvolatile

[†] Michigan State University.
[‡] Department of Chemistry, Northwestern University.
[§] Department of Physics and Astronomy, Northwestern University.

(1) Garin, J.; Parthe, E. *Acta Crystallogr. B* **1972**, *28*, 3672−3674.
(2) Francisco, R. H. P.; Tepe, T.; Eckert, H. *J. Solid State Chem.* **1993**, *107*, 452−459.
(3) (a) Chondroudis, K.; Kanatzidis, M. G. *Inorg. Chem.* **1995**, *34*, 5401−5402. (b) Mccarthy, T. J.; Kanatzidis, M. G. *Chem. Mat.* **1993**, *5*, 1061−1063. (c) Chondroudis, K.; Mccarthy, T. J.; Kanatzidis, M. G. *Inorg. Chem.* **1996**, *35*, 840−844.
(4) Chondroudis, K.; Kanatzidis, M. G. *Inorg. Chem.* **1998**, *37*, 2582−2584.
(5) Chung, I.; Karst, A. L.; Weliky, D. P.; Kanatzidis, M. G. *Inorg. Chem.* **2006**, *45*, 2785−2787.
(6) Chung, I.; Do, J.; Canlas, C. G.; Weliky, D. P.; Kanatzidis, M. G. *Inorg. Chem.* **2004**, *43*, 2762−2764.
(7) (a) Chondroudis, K.; Kanatzidis, M. G. *Angew. Chem., Int. Ed. Engl.* **1997**, *36*, 1324−1326. (b) Chung, I.; Kanatzidis, M. G., unpublished work.
(8) Kanatzidis, M. G. *Curr. Opin. Solid State Mater. Sci.* **1997**, *2*, 139−149.

10.1021/ja075096c CCC: $37.00

phase-change memory.[9,10] The most interesting materials are those with stoichiometric composition because they can switch between the two states without complications due to compositional changes.

At low-temperature $K_2P_2Se_6$ (but not $Rb_2P_2Se_6$) undergoes a phase transition to a structure of lower symmetry while retaining the helical structure. Polar structure $K_2P_2Se_6$ exhibits remarkably strong second harmonic generation (SHG) intensity. In the infrared region the material is highly transmissive over a wide wavelength range. Compared to the SHG intensity of the chalcopyrite compound $AgGaSe_2$, which is the top infrared NLO material used commercially, $K_2P_2Se_6$ exhibited a 50-fold stronger response as well as a type-I phase matching property making it a potential contender material for applications in the IR region. To our best knowledge this is one of the largest NLO SHG responses ever reported for this near- and mid-infrared region of the spectrum. Glassy $K_2P_2Se_6$ also exhibited an SHG response. Since homogeneous glasses generally do not show SHG due to the macroscopically present inversion center, this observation is not only a rare example of amorphous NLO response with no specific treatment such as poling but also of interest for further investigations in optical devices.

2. Experimental Section

2.1. Reagents. The reagents mentioned in this work were used as obtained: K metal (analytical reagent, Aldrich Chemical Co., Milwaukee, WI); Rb metal (analytical reagent, Johnson Matthey/AESAR Group, Seabrook, NH); red phosphorus powder (−100 mesh, Morton Thiokol, Inc., Danvers, MA); Se (99.9999%; Noranda Advanced Materials, Quebec, Canada); *N*,*N*-dimethylformamide (Spectrum Chemicals, ACS reagent grade); diethyl ether (Columbus Chemical Industries, Columbus WI, ACS reagent grade, anhydrous). A_2Se (A = K and Rb) starting materials were prepared by reacting stoichiometric amounts of the elements in liquid ammonia. P_2Se_5 was prepared by heating the mixture of P and Se with a stoichiometric ratio sealing in an evacuated silica tube at 460 °C for 24 h.

2.2 Synthesis. Pure $K_2P_2Se_6$ and $Rb_2P_2Se_6$ were obtained in quantitative yield by heating a mixture of K_2Se/P_2Se_5 = 1:1 and $Rb_2Se/P/Se$ = 1:2.4:5 in an evacuated and sealed silica tube at 450 °C for 3 d followed by cooling at a rate of 5°/h to 250 °C, respectively. After washing with *N*,*N*-dimethylformamide (DMF) and ether, we obtained pure red/orange thick plate-typed single crystals. Energy dispersive spectroscopy (EDS) analysis of the crystals showed an average composition of "$K_2P_{1.9}Se_{5.8}$" and "$Rb_2P_{1.9}Se_{5.9}$". The glassy phases of $K_2P_2Se_6$ and $Rb_2P_2Se_6$ were prepared from a mixture of K_2Se/P_2Se_5 = 1:1 and $Rb_2P_2Se_6$ crystals, respectively, placed in a silica tube and melted at 800−900 °C for 1−2 min with subsequent quenching in ice water. The crystalline compounds were air-stable for at least a week and stable under polar solvents such as DMF, *N*-methylformamide, methyl and ethyl alcohol, and H_2O. Glassy $K_2P_2Se_6$ and $Rb_2P_2Se_6$ were soluble in DMF and methyl alcohol without stirring to give clear light orange solution.

2.3. Physical Measurements.

2.3.1. X-ray Powder Diffraction and Pair Distribution Function (PDF) Analysis. Phase purity X-ray diffraction analyses were performed using a calibrated CPS 120 INEL X-ray powder diffractometer (Cu Kα graphite monochromatized radiation) operating at 40 kV/20 mA and equipped with a position-sensitive detector with flat sample geometry.

The powder X-ray diffraction data for PDF analysis of the crystalline and glassy $K_2P_2Se_6$ were collected at room temperature using an Inel CPS 120 diffractometer. A graphite monochromatized and Rh filtered Ag Kα (0.560 80 Å) radiation was used for the crystalline and glassy $K_2P_2Se_6$, respectively. The samples were ground to a fine powder under a nitrogen atmosphere, loaded into 0.5 mm capillaries, and flame sealed. Fluorescence due to selenium atoms was successfully filtered out by using a 0.150 mm thick bronze foil in front of the CPS detector. Data reduction and the calculation of the PDF were performed as described elsewhere[11] with the PDFGetX2 software.[12]

2.3.2. Electron Microscopy. Semiquantitative analyses of the compounds were performed with a JEOL JSM-35C scanning electron microscope (SEM) equipped with a Tracor Northern energy dispersive spectroscopy (EDS) detector.

2.3.3. Solid-State UV−vis Spectroscopy. Optical diffuse reflectance measurements were performed at room temperature using a Shimadzu UV-3101 PC double-beam, double-monochromator spectrophotometer operating in the 200−2500 nm region using a procedure described in detail elsewhere.[13]

2.3.4. Raman Spectroscopy. Raman spectra were recorded on a Holoprobe Raman spectrograph equipped with a CCD camera detector using 633 nm radiation from a HeNe laser for excitation and a resolution of 4 cm^{-1}. Laser power at the sample was estimated to be about 5 mW, and the focused laser beam diameter was ca. 10 μm. A total of 128 scans was sufficient to obtain good quality spectra.

2.3.5. Infrared Spectroscopy. FT-IR spectra were recorded as solids in a CsI or KBr matrix. The samples were ground with dry CsI or KBr into a fine powder and pressed into translucent pellets. The spectra were recorded in the far-IR region (600−100 cm^{-1}, 4 cm^{-1} resolution) and mid-IR region (500−4000 cm^{-1}, 4 cm^{-1} resolution) with the use of a Nicolet 740 FT-IR spectrometer equipped with a TGS/PE detector and silicon beam splitter.

2.3.6. Differential Thermal Analysis (DTA). Experiments were performed on a Shimadzu DTA-50 thermal analyzer. A sample (∼30 mg) of ground crystalline material was sealed in a silica ampule under vacuum. A similar ampule of equal mass filled with Al_2O_3 was sealed and placed on the reference side of the detector. The sample was heated to 600 °C at 10 °C/min, and after 1 min it was cooled at a rate of −10 °C/min to 50 °C. The residues of the DTA experiments were examined by X-ray powder diffraction. Reproducibility of the results was confirmed by running multiple heating/cooling cycles. The melting and crystallization points were measured at a minimum of the endothermic peak and a maximum of the exothermic peak.

2.3.7. Solid-State Nuclear Magnetic Resonance (NMR) Spectroscopy. The room temperature solid-state NMR measurement was taken on a 9.4 T NMR spectrometer (Varian Infinity Plus) using a double resonance magic angle spinning (MAS) probe. The sample was spun at 8.0 kHz using zirconia rotors of 6 mm outer diameter. Bloch decay spectra were taken with the excitation/detection channel tuned to ^{31}P at 161.39 MHz, a 4.5 μs 90° pulse, and a relaxation delay of 3000 s. The spectrum was referenced using 85% H_3PO_4 at 0 ppm.

2.3.8. X-ray Crystallography. The crystal structure was determined by single-crystal X-ray diffraction methods. For $K_2P_2Se_6$, preliminary examination and data collection were performed on a SMART platform diffractometer equipped with a 1K CCD area detector using graphite monochromatized Mo Kα radiation at 173(2) and 298(2) K. A hemisphere of data was collected at 298(2) K using a narrow-frame

(9) (a) Oh, H.-R.; Cho, B.-H.; Cho, W. Y.; Kang, S.; Choi, B.-G.; Kim, H.-J.; Kim, K.-S.; Kim, D.-E.; Kwak, C.-K.; Byun, H.-G.; Jeong, G.-T.; Jeong, H.-S.; Kim, K. *IEEE J. Solid-State Circuits* **2006**, *41*, 122−126. (b) Ohta, T. *J. Optoelectron. Adv. Mat.* **2001**, *3*, 609−626. (c) Ohta, T.; Nishiuchi, K.; Narumi, K.; Kitaoka, Y.; Ishibashi, H.; Yamada, N.; Kozaki, T. *Jpn. J. Appl. Phys. Part 1* **2000**, *39*, 770−774.

(10) (a) Wełnic, W.; Pamungkas, A.; Detemple, R.; Steimer, C.; Blugel, S.; Wuttig, M. *Nat. Mater.* **2006**, *5*, 56−62. (b) Lee, H.; Kim, Y. K.; Kim, D.; Kang, D. H. *IEEE Trans. Magn.* **2005**, *41*, 1034−1036. (c) Kolobov, A. V.; Fons, P.; Frenkel, A. I.; Ankudinov, A. L.; Tominaga, J.; Uruga, T. *Nat. Mater.* **2004**, *3*, 703−708.

(11) Hwang, S. J.; Petkov, V.; Rangan, K. K.; Shastri, S.; Kanatzidis, M. G. *J. Phys. Chem. B* **2002**, *106*, 12453−12458.

(12) Qiu, X. Y.; Bozin, E. S.; Juhas, P.; Proffen, T.; Billinge, S. J. L. *J. Appl. Crystallogr.* **2004**, *37*, 110−116.

(13) Aitken, J. A.; Chondroudis, K.; Young, V. G.; Kanatzidis, M. G. *Inorg. Chem.* **2000**, *39*, 1525−1533.

method with scan widths of 0.30° in ω and an exposure time of 30 s/frame. For the data collected at 173(2) K, an exposure time of 60 s/frame was used. The data were integrated using the SAINT program. An analytical absorption and empirical absorption correction using the program SADABS were performed for both sets. The initial positions for all atoms were obtained using direct methods, and the structures were refined with the full-matrix least-squares techniques of the SHELXTL[14] crystallographic software package. Crystallographic data are given in Table 1. Satisfactory refinement was obtained with the chiral space group, $P3_121$ at 298(2) K and $P3_1$ at 173(2) K (Tables 2−4). The crystals used for structure refinement were racemically and merohedrally twinned, and the twinning fractions were refined to 49.5, 25.8, 23.1, and 1.6% at 173(2) K. The racemic and merohedral twinning behavior was typical for $K_2P_2Se_6$, and their relative ratios determined for several crystals were very similar. Interestingly, flux synthesis using the mixture of $K_2Se/P/Se = 1:2.4:5$ significantly increased the portion of one enantiomorph compared to the crystals obtained with a direct combination reaction of K_2Se and P_2Se_5. The racemic ratio improved from 1:1 to 3:1.

Intensity data for $Rb_2P_2Se_6$ were collected at 100(2) K on a STOE IPDS II diffractometer with Mo Kα radiation operating at 50 kV and 40 mA with a 34 cm image plate. Individual frames were collected with a 5 min exposure time and a 1.0 ω rotation. The X-AREA, X-RED, and X-SHAPE software package was used for data extraction and integration and to apply empirical and analytical absorption corrections. The SHELXTL software package was used to solve and refine the structure. The most satisfactory refinement was obtained with the chiral space group, $P3_121$ at 100(2) K rather than $P3_221$. The refined Flack x parameter was 0.901(96). After inversion to $P3_121$, the Flack

Table 1. Crystallographic Refinement Details for $K_2P_2Se_6$ and $Rb_2P_2Se_6$

formula	$K_2P_2Se_6$	$K_2P_2Se_6$	$Rb_2P_2Se_6$
space group	$P3_121$ (no. 152)	$P3_1$ (no. 144)	$P3_121$ (no. 152)
a, b, Å	7.2746(8)	14.4916(7)	7.2982(5)
c, Å	18.870(4)	18.800(2)	19.002(2)
α, β (deg)	90	90	90
γ (deg)	120	120	120
Z	3	12	3
V, Å^3	864.8(2)	3419.2(4)	876.5(1)
d (calculated), gr/cm^3	3.536	3.578	4.016
temperature, K	298(2)	173(2)	101(2)
λ, Å	0.710 73	0.710 73	0.710 73
μ, mm^{-1}	19.974	20.209	27.272
F(000)	816	3264	924
θ_{max} (deg)	28.27	28.29	30.99
total reflections	7444	21703	9968
total unique reflections	1382	10294	1866
no. parameters	47	365	49
refinement method	full-matrix least-squares on F^2		
final R indices [$I > 2\sigma(I)$], R1[a]/wR2[b] (%)	2.69/5.89	4.61/8.17	3.87/4.56
R indices (all data), R1/wR2	3.10/6.04	4.92/11.43	4.74/4.70
goodness-of-fit on F^2	1.078	0.748	0.976
absolute structure parameter	0.27(2)	0.25(1)	0.08(3)

[a] $R1 = \Sigma\,||F_o| - |F_c||/\Sigma|F_o|$. [b] $wR2 = \{\Sigma\,[w(F_o^2 - F_c^2)^2]/\Sigma\,[w(F_o^2)^2]\}^{1/2}$.

Table 2. Selected Bond Distances (Å) and Angles (deg) for $K_2P_2Se_6$ at 298(2) K

P−P	2.242(2)	Se(1)−P−Se(2)	111.88(6)
P−Se(1)	2.329(1)	Se(1)−P−Se(3)	112.29(6)
P−Se(2)	2.131(2)	Se(2)−P−Se(3)	117.95(6)
P−Se(3)	2.128(1)	P−Se(1)−Se(1)	100.55(4)
Se(1)−Se(1)	2.337(1)	P−P−Se(1)	93.85(7)
		P−P−Se(2)	111.42(4)
		P−P−Se(3)	106.69(5)

Table 3. Selected Bond Distances (Å) and Angles (deg) for $K_2P_2Se_6$ at 173(2) K

P(1)−P(2)	2.227(17)	P(7)−Se(21)	2.126(17)
P(3)−P(4)	2.27(3)	P(8)−Se(22)	2.113(16)
P(5)−P(6)	2.236(18)	P(8)−Se(23)	2.131(16)
P(7)−P(8)	2.23(3)	P(8)−Se(24)	2.368(17)
P(1)−Se(1)	2.297(17)	Se(1)−Se(18)	2.334(13)
P(1)−Se(2)	2.141(17)	Se(6)−Se(7)	2.330(8)
P(1)−Se(3)	2.154(17)	Se(12)−Se(13)	2.342(7)
P(2)−Se(4)	2.118(17)	Se(19)−Se(24)	2.347(12)
P(2)−Se(5)	2.151(17)	Se(1)−P(1)−Se(2)	113.6(7)
P(2)−Se(6)	2.346(17)	Se(1)−P(1)−Se(3)	111.1(7)
P(3)−Se(7)	2.305(17)	Se(2)−P(1)−Se(3)	116.8(8)
P(3)−Se(8)	2.138(17)	Se(4)−P(2)−Se(5)	120.0(7)
P(3)−Se(9)	2.119(18)	Se(4)−P(2)−Se(6)	112.8(8)
P(4)−Se(10)	2.123(17)	Se(5)−P(2)−Se(6)	109.4(7)
P(4)−Se(11)	2.133(18)	Se(7)−P(3)−Se(8)	113.9(7)
P(4)−Se(12)	2.356(17)	Se(7)−P(3)−Se(9)	112.9(7)
P(5)−Se(13)	2.286(17)	Se(8)−P(3)−Se(9)	116.5(8)
P(5)−Se(14)	2.140(17)		
P(5)−Se(15)	2.155(16)		
P(6)−Se(16)	2.157(15)		
P(6)−Se(17)	2.129(16)		
P(6)−Se(18)	2.363(17)		
P(7)−Se(19)	2.309(17)		
P(7)−Se(20)	2.125(17)		

(14) *SMART, SAINT, SHELXTL: Data Collection and Processing Software for the SMART-CCD System*; Siemens Analytical X-ray Instruments Inc.: Madison, WI, 1997.
(15) Gieck, C.; Derstroff, V.; Block, T.; Felser, C.; Regelsky, G.; Jepsen, O.; Ksenofontov, V.; Gutlich, P.; Eckert, H.; Tremel, W. *Chem.—Eur. J.* **2004**, *10*, 382−391.
(16) Gieck, C.; Tremel, W. *Chem.—Eur. J.* **2002**, *8*, 2980−2987.
(17) (a) Canadell, E.; Rachidi, I. E. I.; Pouget, J. P.; Gressier, P.; Meerschaut, A.; Rouxel, J.; Jung, D.; Evain, M.; Whangbo, M. H. *Inorg. Chem.* **1990**, *29*, 1401−1407. (b) *Electronic Properties of Inorganic Quasi-One-Dimensional Compounds*; Monceau, P., Ed.; D. Reidel Publishing Company: Dordrecht, 1985.
(18) Kanatzidis, M. G.; Sutorik, A. C. *Prog. Inorg. Chem.* **1995**, *43*, 151−265.
(19) Canlas, C. G.; Kanatzidis, M. G.; Weliky, D. P. *Inorg. Chem.* **2003**, *42*, 3399−3405.
(20) (a) Chrissafis, K.; Kyratsi, T.; Paraskevopoulos, K. M.; Kanatzidis, M. G. *Chem. Mater.* **2004**, *16*, 1932−1937. (b) Kyratsi, T.; Chrissafis, K.; Wachter, J.; Paraskevopoulos, K. M.; Kanatzidis, M. G. *Adv. Mater.* **2003**, *15*, 1428−1431. (c) Wachter, J. B.; Chrissafis, K.; Petkov, V.; Malliakas, C. D.; Blic, D.; Kyratsi, T.; Paraskevopoulos, K. M.; Manhanti, S. D.; Torbrugge, T.; Eckert, H.; Kanatzidis, M. G. *J. Solid State Chem.* **2007**, *180*, 420−431.
(21) Dhingra, S.; Kanatzidis, M. G. *Science* **1992**, *258*, 1769−1772.
(22) (a) Maeda, Y.; Andoh, H.; Ikuta, I.; Minemura, H. *J. Appl. Phys.* **1988**, *64*, 1715−1719. (b) Feinleib, J.; Deneufvi, J.; Moss, S. C.; Ovshinsk.Sr *Appl. Phys. Lett.* **1971**, *18*, 254−257.
(23) (a) Pätzmann, U.; Brockner, W. *Z. Naturforsch., A* **1987**, *42*, 515−516. (b) Brockner, W.; Ohse, L.; Pätzmann, U.; Eisenmann, B.; Schäfer, H. *Z. Naturforsch., A* **1985**, *40*, 1248−1252.
(24) Aitken, J. A.; Evain, M.; Iordanidis, L.; Kanatzidis, M. G. *Inorg. Chem.* **2002**, *41*, 180−191.
(25) (a) Choi, K. S.; Kanatzidis, M. G. *Chem. Mater.* **1999**, *11*, 2613−2618. (b) Evain, M.; Queignec, M.; Brec, R.; Sourisseau, C. *J. Solid State Chem.* **1988**, *75*, 413−431. (c) Butler, I. S.; Harvey, P. D.; Mccall, J. M.; Shaver, A. *J. Raman Spectrosc.* **1986**, *17*, 221−228.
(26) (a) Billinge, S. J. L.; Kanatzidis, M. G. *Chem. Commun.* **2004**, 749−760. (b) Petkov, V.; Billinge, S. J. L.; Shastri, S. D.; Himmel, B. *Phys. Rev. Lett.* **2000**, *85*, 3436.
(27) Nikogosyan, D. N. *Nonlinear optical crystals: a complete survey*; Springer-Science: New York, 2005.
(28) Liao, J. H.; Marking, G. M.; Hsu, K. F.; Matsushita, Y.; Ewbank, M. D.; Borwick, R.; Cunningham, P.; Rosker, M. J.; Kanatzidis, M. G. *J. Am. Chem. Soc.* **2003**, *125*, 9484−9493.
(29) Hanko, J. A.; Kanatzidis, V. G. *J. Solid State Chem.* **2000**, *151*, 326−329.
(30) Aitken, J. A.; Marking, G. A.; Evain, M.; Iordanidis, L.; Kanatzidis, M. G. *J. Solid State Chem.* **2000**, *153*, 158−169.
(31) Chondroudis, K.; Hanko, J. A.; Kanatzidis, M. G. *Inorg. Chem.* **1997**, *36*, 2623−2632.
(32) (a) Dougherty, J. P.; Kurtz, S. K. *J. Appl. Crystallogr.* **1976**, *9*, 145−158. (b) Kurtz, S. K.; Perry, T. T. *J. Appl. Phys.* **1968**, *39*, 3798−3813.
(33) Choy, M. M.; Byer, R. L. *Phys. Rev. B* **1976**, *14*, 1693−1706.
(34) Antonyuk, B. P.; Antonyuk, V. B. *Opt. Commun.* **1998**, *147*, 143−147.
(35) (a) Fokine, M.; Saito, K.; Ikushima, A. J. *Appl. Phys. Lett.* **2005**, *87*, 171907. (b) Kityk, I. V. *J. Phys. Chem. B* **2003**, *107*, 10083−10087. (c) Qiu, M. X.; Pi, F.; Orriols, G. *Appl. Phys. Lett.* **1998**, *73*, 3040−3042. (d) Fujiwara, T.; Takahashi, M.; Ikushima, A. J. *Appl. Phys. Lett.* **1997**, *71*, 1032−1034.
(36) Iseler, G. W. *J. Cryst. Growth* **1977**, *41*, 146−150.
(37) Korczak, P.; Staff, C. B. *J. Cryst. Growth* **1974**, *24*, 386−389.

Table 4. K−Se Distances in $K_2P_2Se_6$ at 173(2) K with Standard Deviation in Parentheses[a,b]

K(1)−Se(17)	3.345(14)	K(5)−Se(5)#5	3.321(15)
K(1)−Se(14)	3.361(17)	K(5)−Se(10)	3.351(15)
K(1)−Se(8)#12	3.363(17)	K(5)−Se(20)#7	3.352(15)
K(1)−Se(20)#7	3.391(16)	K(5)−Se(3)#5	3.367(15)
K(1)−Se(23)	3.456(16)	K(5)−Se(23)	3.481(15)
K(1)−Se(12)#9	3.473(16)	K(5)−Se(7)#12	3.484(15)
K(1)−Se(10)	3.554(14)	K(5)−Se(2)#5	3.606(15)
K(1)−Se(24)	3.842(17)	K(5)−Se(19)#5	3.888(16)
K(2)−Se(20)#2	3.310(17)	K(6)−Se(11)#9	3.307(15)
K(2)−Se(4)#3	3.360(16)	K(6)−Se(17)#11	3.329(16)
K(2)−Se(11)	3.433(17)	K(6)−Se(21)#11	3.339(15)
K(2)−Se(9)#5	3.393(17)	K(6)−Se(5)#11	3.344(15)
K(2)−Se(21)	3.358(17)	K(6)−Se(2)#6	3.423(16)
K(2)−Se(22)	3.595(16)	K(6)−Se(13)	3.433(15)
K(2)−Se(24)	3.462(16)	K(6)−Se(15)	3.547(14)
K(2)−Se(12)	3.940(16)	K(6)−Se(1)#9	3.849(15)
K(3)−Se(22)	3.317(16)	K(7)−Se(10)	3.309(14)
K(3)−Se(3)#5	3.317(17)	K(7)−Se(2)#6	3.325(15)
K(3)−Se(9)	3.348(17)	K(7)−Se(15)#12	3.363(15)
K(3)−Se(16)	3.348(15)	K(7)−Se(5)#6	3.398(15)
K(3)−Se(14)#5	3.505(16)	K(7)−Se(2)#5	3.470(15)
K(3)−Se(6)	3.509(16)	K(7)−Se(18)#9	3.473(14)
K(3)−Se(23)	3.582(15)	K(7)−Se(11)#9	3.616(15)
K(3)−Se(18)	3.915(16)	K(7)−Se(6)	3.811(14)
K(4)−Se(23)	3.341(14)	K(8)−Se(8)#10	3.318(14)
K(4)−Se(22)#4	3.345(14)	K(8)−Se(16)#10	3.325(14)
K(4)−Se(15)	3.359(15)	K(8)−Se(4)#4	3.346(14)
K(4)−Se(9)	3.388(15)	K(8)−Se(14)	3.380(15)
K(4)−Se(19)	3.483(15)	K(8)−Se(16)#4	3.420(15)
K(4)−Se(11)#4	3.509(16)	K(8)−Se(1)#10	3.478(14)
K(4)−Se(14)	3.646(15)	K(8)−Se(3)	3.518(15)
K(4)−Se(7)	3.836(15)		

[a] The maximum threshold for bond distances is 3.750 Å. The coordination number of K atoms was determined to be seven. [b] Symmetry transformations used to generate equivalent atoms: (#1) $x+1, y, z$; (#2) $x+1, y+1, z$; (#3) $x, y+1, z$; (#4) $-x+y+1, -x+2, z-1/3$; (#5) $-y+2, x-y+1, z+1/3$; (#6) $x, y-1, z$; (#7) $-y+1, x-y+1, z+1/3$; (#8) $-x+y+1, -x+1, z-1/3$; (#9) $x-1, y-1, z$; (#10) $x-1, y, z$; (#11) $-x+y, -x+1, z-1/3$; (#12) $-y+1, x-y, z+1/3$.

parameter x was 0 and the BASF value was 0.89. Following refinement for racemic and merohedral twinning done at the same time, the twinning fractions were refined to 89.43, 5.83, 5.59, and 2.15% and x parameter 0.0. $Rb_2P_2Se_6$ did not show a phase transition with temperature change, and its crystal structure is the same as that of $K_2P_2Se_6$ at room temperature (RT). The parameters for data collection and the details of the structural refinement are given in Table 1. Fractional atomic coordinates and displacement parameters for each structure are given in the Supporting Information. In all cases the atoms were refined to full occupancy.

2.3.9. Nonlinear Optical Property Measurements. We used the frequency-tripled output of a passive-active mode-locked Nd:YAG laser with a pulse width of about 15 ps and a repetition rate of 10 Hz to pump an optical parametric amplifier (OPA). The OPA generates vertically polarized pulses in the ranges 400−685 nm and 737−3156 nm. In order to check the SHG efficiency as a function of the excitation energy, we tuned the wavelength of the incident light from 1000 to 2000 nm. In this range, the spectral bandwidth of the linearly polarized light from the OPA is rather broad, about 2 meV full width at half-maximum. However, the phase space compression phenomena ensure effective SHG where lower energy portions are exactly compensated by higher parts thereby satisfying both energy and momentum conservation. The incident laser pulse of 300 μJ was focused onto a spot 500 μm in diameter using a 3 cm focal-length lens. The corresponding incident photon flux was about 10 GW/cm^2. The SHG signal was collected in a reflection geometry from the excitation surface and focused onto a fiber optic bundle. The output of the fiber optic bundle was coupled to the entrance slit of a Spex Spec-One 500 M spectrometer and detected using a nitrogen-cooled CCD camera. The data collection time was 20 s.

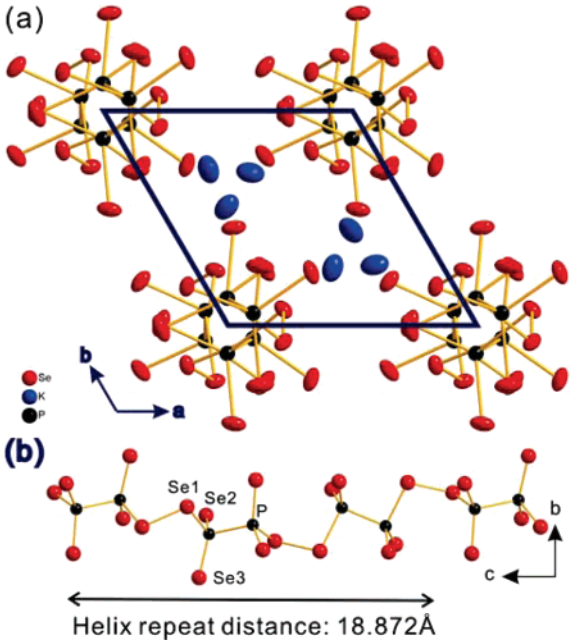

Figure 1. Structure of $K_2P_2Se_6$ at 298(2) K. (a) The unit cell viewed down the c-axis. The thermal ellipsoids with 30% probability are shown. (b) View of a $^1_\infty[P_2Se_6^{2-}]$ chain looking down the a-axis. A helix forms by three $[P_2Se_6]$ units and repeats itself at every 18.872 Å.

3. Results and Discussion

3.1. Crystal Structure. Because at RT $K_2P_2Se_6$ and $Rb_2P_2Se_6$ are isostructural, the description that follows will be concentrated on the K salt. The structure has infinitely extended helical chains parallel to the c-axis; see Figure 1a. The chains are composed of ethane-like $[P_2Se_6]$ repeat units that are linked via terminal Se−Se linkages to give infinite helices of $^1_\infty[P_2Se_6^{2-}]$, Figure 1b. The chirality of $K_2P_2Se_6$ is preserved in the crystal, and at RT the compound adopts the chiral trigonal space group, $P3_121$. Helical features have been described in the quaternary thiophosphates $ANb_2P_2S_{12}$ (A = K, Rb, Cs)[15] and $A_{11}U_7(PS_4)_{13}$ (A = K, Rb),[16] but $K_2P_2Se_6$ is the first example to display an infinite helix structure of free-standing chalcophosphate anions.

The unit cell contains a single crystallographically unique strand of the chain. Each helix runs with identical handedness along the c-axis. Because the helix is generated by a crystallographic 3_1 screw axis along the c-direction, each coil of the helix in the unit cell includes three P_2Se_6 units. There is a single crystallographic P site in the structure, and pitch of the helix is 18.872(4) Å, corresponding to the unit cell repeat distance along the c-axis. The interspiral distance is equal to the a-lattice constant of the unit cell. Projected along its axis, a chiral 1D channel is seen with a cross-section diameter of ~1.17 Å. The P−P bond distance is normal at 2.242(2) Å. P−Se bond distances range from 2.126(1) to 2.329(1) Å comparable to known values. The P−Se−Se−P dihedral angle of 88.55(1)°,

(38) Kozhina, I. I.; Borshchevskii, A. S. *Vestnik Leningradskogo Universiteta, Seriya 4: Fizika, Khimiya* **1971**, 87−92.
(39) Feigelson, R. S.; Route, R. K. *Opt. Eng.* **1987**, *26*, 113−19.

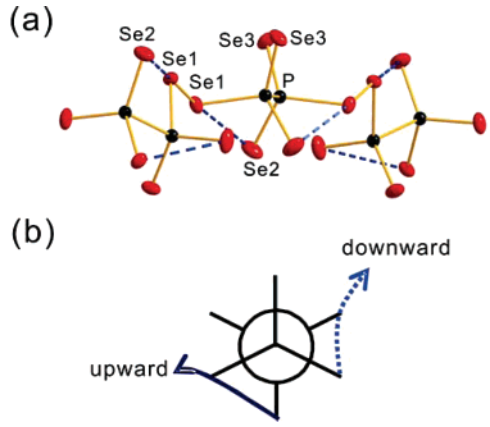

Figure 2. (a) Projection view of a $^1_\infty[P_2Se_6^{2-}]$ chain slightly slanted in order to show the staggered *anti*-conformation of $[P_2Se_6]$. The role of short Se···Se nonbonding interactions (dashed line) along a helix segment is shown. Se(1)···Se(2), 3.559(1) Å. (b) Projection through P−P bonding showing the relationship between short Se···Se nonbonding interaction and chain propagation.

almost 90°, causes a relatively short Se−Se bond distance of 2.337(1) Å compared to those in $KPSe_6$.[6] The ethane-like P_2Se_6 repeat unit adopts a local *anti*-conformation to minimize the steric hindrance around the P−P bond created by the helical geometry, Figure 2a. The unit is also distorted from the ideal geometry with the Se−P−Se angles ranging from 111.88(6)° to 117.95(6)°.

It is noteworthy to point out the unusually short Se···Se nonbonding interaction that is observed at 3.559(1) Å for Se1···Se2, Figure 2a. This is shorter than the van der Waals radii sum of 3.80 Å and probably meaningful in stabilizing the crystal structure. Because the P_2Se_6 fragment is intrinsically centrosymmetric, the helical architecture results from the conformation of the selenophosphate chain. In this regard, the short Se···Se contacts likely play a critical role in forming the coil by maximizing Se pπ orbital overlap through Se2···Se1−Se1···Se2 connections, Figure 2. To minimize the repulsion force between them, each $[P_2Se_6]$ subunit rotates along the Se2···Se1−Se1···Se2 connection as an axis and consequently achieves the helical form. In fact, the Se3−P−P−Se3 torsion angle is severely compressed to only 36.23(1)°. Similarly short Se···Se interactions are well-known in other chalcogenide systems. In $Rb_4P_6Se_{12}$[5] and $APSe_6$,[6] for example, these interactions act to form pseudo one- or two-dimensional structures, respectively. The low-dimensional charge density wave compound $NbSe_3$[17] also has similar interactions.

3.2. Low-Temperature Structure. We discovered that when cooled $K_2P_2Se_6$ undergoes a displacive phase transition to lower symmetry with no bond breaking at lower temperature. The $P3_1$-21 space group at room temperature was lowered to $P3_1$ at 173 K by losing twofold symmetry perpendicular to *a*- and *b*-axis, Figure 3a. The new cell was enlarged to a $2a \times 2b \times c$ supercell. $P3_1$ is a maximal non-isomorphic subspace group of $P3_121$. As a result, the crystallographically unique K and P atoms and three independent Se atoms in $K_2P_2Se_6$ split to 8, 8, and 24 independent atoms, respectively. The resulting four helixes in the unit cell are differentiated crystallographically into two groups as denoted by A and B in Figure 3a and b with a ratio of 3:1. It is noted that K7 and K8 still generate themselves by a threefold screw axis surrounded by three identical strands of $^1_\infty[P_2Se_6^{2-}]$ of type A. On the other hand, K1−K6 are

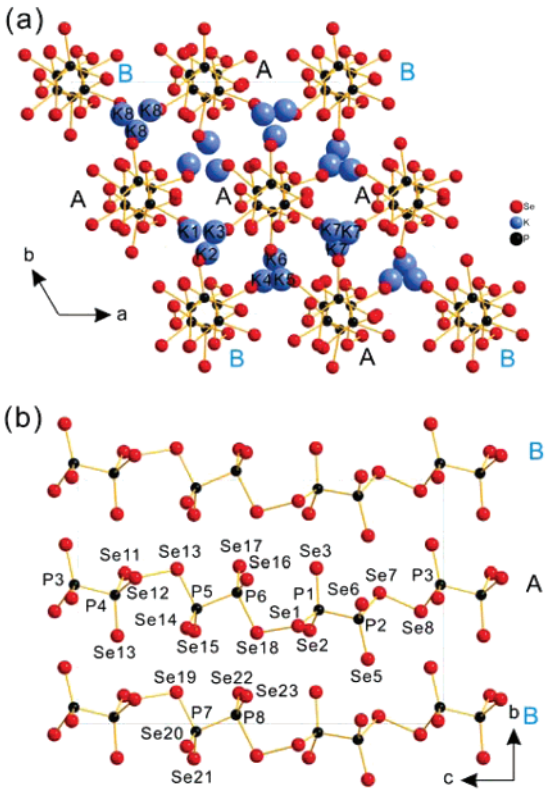

Figure 3. Structure of $K_2P_2Se_6$ at 173(2) K. (a) The unit cell viewed down the *c*-axis showing the superstructure. Crystallographically unique chains are differentiated as A and B. K atoms are labeled. (b) View of $^1_\infty[P_2Se_6^{2-}]$ chains with labeling down the *a*-axis. K atoms are omitted for clarity.

crystallographically unique and generated by a 3_1 screw and 2-fold rotation operation perpendicular to *a*- and *b*-axes. They are surrounded by two A and one B strands.

$Rb_2P_2Se_6$ did not show such a structural transition on cooling down to 100 K. The different behavior can be understood by the alkali metal size effect. The most notable change in going from the $P3_121$ to $P3_1$ for the K analogue is found in the coordination environment of the K atoms. At room temperature K atoms are coordinated by six closely lying Se atoms, whereas this expands to seven at low temperature, Figure 4. This is reminiscent of a pressure effect imposed on the structure as the unit cell contracts with falling temperature. Therefore the driving force for the transition seems to be the formation of the extra K···Se bonds. This effect seems to be absent in the Rb analogue as the coordination environment of these atoms is already high at room temperature involving 10 Se atoms. Tables 4−7 show a comparison of the K···Se and Rb···Se distances in the two structures for both room and low temperature.

3.3. Synthesis, Reaction Chemistry, and Characterization. The alkali metal chalcophosphate ternary system is highly attractive as a model system to probe how flux conditions influence the synthetic outcome and the structure of a resulting compound.[5] A reaction medium forms by simple *in situ* fusion of A_2Q/P_2Q_5 or P/Q, and this flux is conceptually defined as $A_xP_yQ_z$. The basicity of the flux is determined by the A/P/Q ratio. Higher A/P ratios impart stronger basicity to the flux. Lower A/Q ratios produce lower basicity, etc. Alternatively, for the same A/P ratio the basicity can be increased in going from the smaller to the larger alkali atoms. Therefore both the A/P ratio and the nature of the A atoms could be conveniently

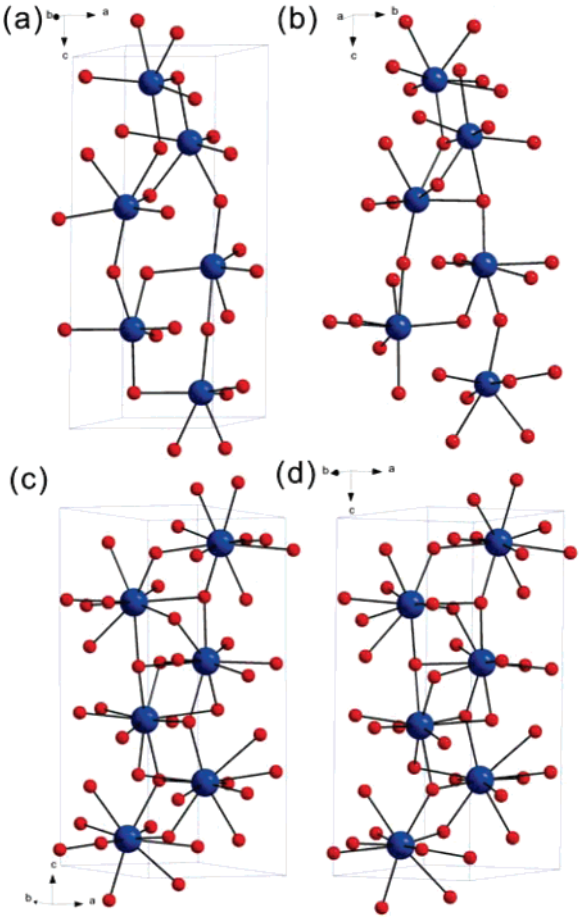

Figure 4. The coordination environment of K atoms in $K_2P_2Se_6$ is six at 298(2) K (a) and expands to seven at 173(2) K (b). The coordination environment of Rb atoms in $Rb_2P_2Se_6$ at (c) 298(2) K and (d) 100(2) K. It remains unchanged at both temperatures where Rb is coordinated to 10 Se atoms. Large blue spheres are K or Rb atoms, and small black ones are Se atoms. P atoms are omitted for clarity.

Table 5. K−Se Distances in $K_2P_2Se_6$ at 273(2) K with Standard Deviation in Parentheses[a,b]

K−Se(2)	3.3367(18)	K−Se(1)#1	3.4834(17)
K−Se(3)#6	3.3388(18)	K−Se(2)#2	3.8395(19)
K−Se(3)#2	3.3695(19)	K−Se(1)#4	3.8731(18)
K−Se(2)#4	3.4263(18)	K−Se(3)#1	3.9244(19)
K−Se(2)#7	3.4537(17)		

[a] The maximum threshold for bond distances is 3.750 Å. The coordination number of K atoms was determined to be six. [b] Symmetry transformations used to generate equivalent atoms: (#1) $-x, -x + y, -z + 1/3$; (#2) $-x - 1, -x + y - 1, -z + 1/3$; (#3) $-x + y - 2, -x, z - 1/3$; (#4) $-x - 1, -x + y, -z + 1/3$; (#5) $-x + y - 1, -x + 1, z - 1/3$; (#6) $-y + 1, x - y + 2, z + 1/3$; (#7) $-y, x - y + 2, z + 1/3$; (#8) $x - y + 1, -y + 2, -z + 2/3$; (#9) $y - 1, x + 1, -z$.

used as a key reaction parameter to control the formation of a product from being a simple molecular species to being a more complex discrete or extended structure. For example to obtain the classical molecular salts A_3PSe_4 and $A_4P_2Se_6$ (A = alkali metal), high ratios of A_2Se/P_2Se_5 (>2:1) are required.

The polymeric $K_2P_2Se_6$ is realized under less basic conditions, namely with K_2Se/P_2Se_5 = 1:1, than the typical ternary alkali selenophosphates with molecular structures. In fact, less basic conditions or lower flux temperatures tend to generate longer or extended fragments.[18] This could explain why more basic Rb or Cs analogues to $K_2P_2Se_6$ could not be obtained from identical reaction conditions. The slightly higher basic character

Table 6. Rb−Se Distances in $Rb_2P_2Se_6$ at 100(2) K with Standard Deviation in Parentheses[a,b]

Rb−Se(3)	3.4778(12)	Rb−Se(2)#7	3.5101(12)
Rb−Se(2)	3.5715(13)	Rb−Se(2)#10	3.7393(13)
Rb−Se(1)	3.6011(13)	Rb−Se(2)#8	3.7754(13)
Rb−Se(3)#1	3.4248(12)	Rb−Se(1)#5	3.8599(12)
Rb−Se(2)#4	3.4357(11)	Rb−Se(3)#1	3.8706(13)

[a] The maximum threshold for bond distances is 4.000 Å. Rb−Se distance was not found up to 4.500 Å over the threshold. The coordination number of Rb atoms was determined to be 10. [b] Symmetry transformations used to generate equivalent atoms: (#1) $-x + 1, -x + y, -z + 1/3$; (#2) $y, x - 1, -z$; (#3) $-x + 2, -x + y + 1, -z + 1/3$; (#4) $x - 1, y - 1, z$; (#5) $x, y + 1, z$; (#6) $y + 1, x, -z$; (#7) $x + 1, y, z$; (#8) $y + 1, x - 1, -z$; (#9) $x, y - 1, z$; (#10) $x + 1, y + 1, z$; (#11) $x - 1, y, z$; (#12) $-x + 1, -x + y + 1, -z + 1/3$.

Table 7. Rb−Se Distances in $Rb_2P_2Se_6$ at 298(2) K with Standard Deviation in Parentheses[a,b]

Rb−Se(3)	3.4714(23)	Rb−Se(1)	3.6545(22)
Rb−Se(2)	3.4735(25)	Rb−Se(2)#6	3.7805(23)
Rb−Se(3)#11	3.5172(22)	Rb−Se(1)#7	3.8185(22)
Rb−Se(2)#9	3.5481(23)	Rb−Se(1)#5	3.9055(21)
Rb−Se(2)#5	3.6271(23)	Rb−Se(3)#3	3.9302(23)

[a] The maximum threshold for bond distances is 4.000 Å. Rb−Se distance was not found up to 4.500 Å over the threshold. The coordination number of Rb atoms was determined to be 10. [b] Symmetry transformations used to generate equivalent atoms: (#1) $-x + 1, -x + y, -z + 1/3$; (#2) $y, x - 1, -z$; (#3) $-x + 2, -x + y + 1, -z + 1/3$; (#4) $x - 1, y - 1, z$; (#5) $x, y + 1, z$; (#6) $y + 1, x, -z$; (#7) $x + 1, y, z$; (#8) $y + 1, x - 1, -z$; (#9) $x, y - 1, z$; (#10) $x + 1, y + 1, z$; (#11) $x - 1, y, z$; (#12) $-x + 1, -x + y + 1, -z + 1/3$.

of Rb and Cs change the reaction path to a more oxidized chalcophosphates (i.e., the P^{5+} species $RbPSe_6$ and $CsPSe_6$). $Rb_2P_2Se_6$ could be obtained however by adjusting/correcting the flux basicity by adding 0.4 mol of P to the Rb_2Se/P_2Se_5 = 1:1 ratio. This prevents the oxidation for P from 4+ to 5+. Thus it would appear that extended structural motifs for chalcophosphates are more likely to be produced by weak basic fluxes with smaller less Lewis basic alkali metals such as potassium, sodium, and lithium.

Conceptually, $^1_\infty[P_2Se_6^{2-}]$ can be regarded as deriving from oxidative polymerization of the $[P_2Se_6]^{4-}$ anion, see eq 1. Although it was not synthesized in this fashion, we speculate that an actual oxidation in solution, with, e.g., I_2 as the oxidant, may in fact be successful if run under proper conditions.

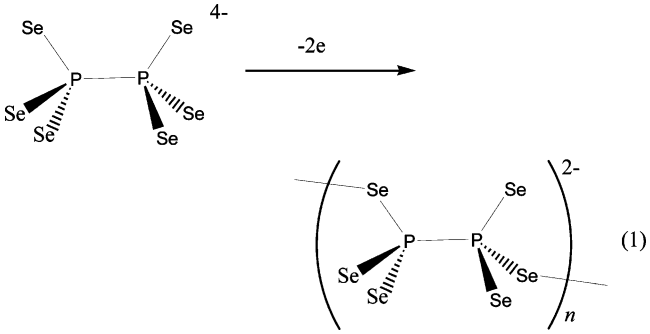

(1)

The polymeric chain is stabilized with no help of coordinating to a metal and represents a rare chalcophosphate anion. The only other example which is stabilized by alkali cations is $^1_\infty[PSe_6^-]$.[6] The latter has PSe_4 tetrahedra condensed with diselenide (Se_2^{2-}) groups.

Finally, the existence of a single crystallographic P site in the RT structure of $K_2P_2Se_6$ is supported by solid state ^{31}P NMR

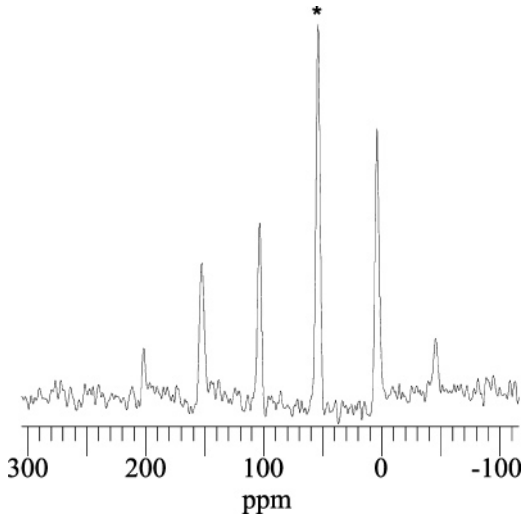

Figure 5. Solid state ^{31}P MAS NMR spectrum of crystalline $K_2P_2Se_6$ at room temperature. The asterisk (*) indicates the isotropic peak.

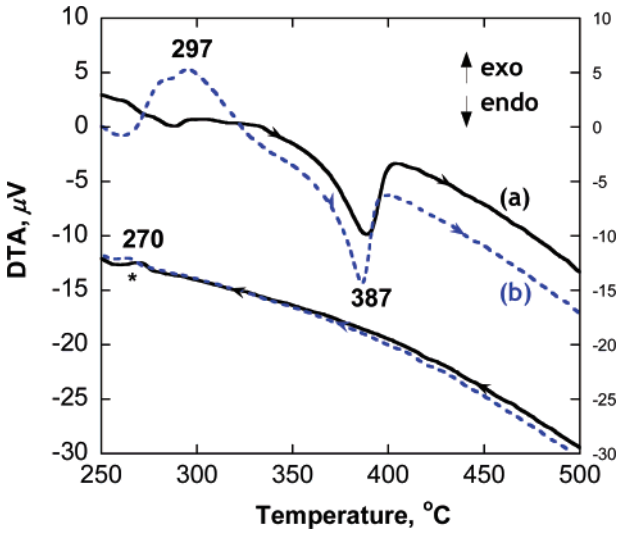

Figure 6. Differential thermal analysis diagram of a sample of $K_2P_2Se_6$. (a) Heating curve showing melting at 387 °C in the first heating cycle (black solid line) with no crystallization upon cooling. (b) Exothermic crystallization followed by melting upon heating in the second cycle (blue dotted line). Asterisk indicates the vitrification event upon cooling.

spectroscopy. Under MAS at RT, crystalline $K_2P_2Se_6$ gave a single isotropic chemical shift (CS) at 54.6 ppm, Figure 5. The result supports the crystal structure of $K_2P_2Se_6$ at room temperature which indicates only one crystallographically unique P atom. The chemical shift value is close to that of $A_2CdP_2Se_6$ (A = K, Rb) and $K_2Cu_2P_4Se_{10}$, all of which include the P_2Se_6-type ligand.[19]

3.4. Glass Formation, Phase-Change Behavior, and Local Structure. Both title compounds described here exhibit reversible phase change behavior. Differential thermal analysis of $K_2P_2Se_6$ performed at a rate of 10 °C/min indicates that the compound melts congruently at 387 °C, Figure 6. Upon cooling it forms a dark red glass at 270 °C. Crystallization is only observed on heating where the glass recrystallizes exothermically at 297 °C. The vitrification is observed again on cooling the melt to room temperature. The powder X-ray diffraction patterns (PXRD) of the pristine and recrystallized sample from DTA were identical confirming the structure recovering ability of this material.

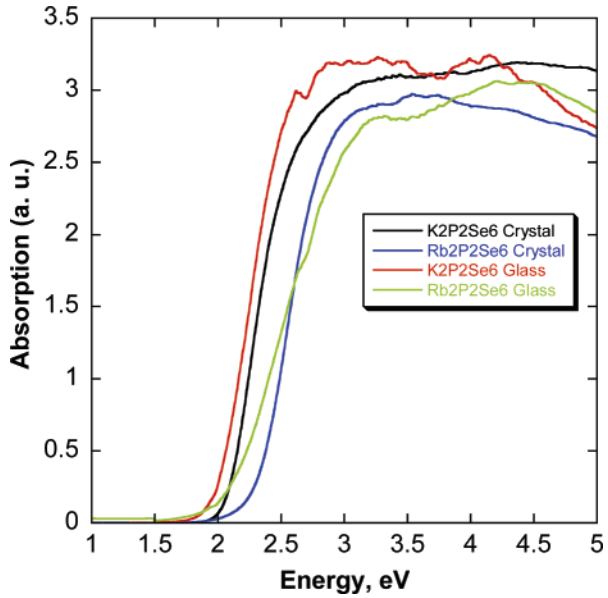

Figure 7. Solid-state UV−vis optical absorption spectra of crystalline and glassy $K_2P_2Se_6$ and $Rb_2P_2Se_6$ showing the red shift in absorption edge in the glass samples. The band gaps are 2.09, 1.98 eV for the K and 2.32, 2.10 eV for Rb analogues, respectively.

The thermal behavior of $Rb_2P_2Se_6$ is different from that of $K_2P_2Se_6$. The DTA carried out at a rate of 10 °C/min revealed the melting at 364 °C on heating and gave a dark red glass at 255 °C on cooling during a first cycle. On a second cycle, no crystallization was observed as the glass could not recover the crystal structure. The melting was observed again at 369 °C followed by vitrification at 255 °C on cooling. The PXRD confirmed the amorphous nature of the glassy sample after the first and second cycles. The amorphous sample recrystallized to a pristine structure only when the heating rate was lowered to less than 5 °C/min. The DTA performed at a rate of 5 °C/min showed melting at 366 °C on heating and subsequent crystallization at 305 °C on cooling. The PXRD of pristine and the sample obtained after each cycle matched perfectly. These results are consistent with a greater glass forming ability of the Rb salt compared to the K salt. This is in agreement with a similar trend identified recently in the series $K_{1-x}Rb_xSb_5S_8$.[20]

The solid-state optical absorption UV−vis spectra of crystalline and glassy $A_2P_2Se_6$ show sharp absorption edges, Figure 7. The band gap of crystalline and glassy phases was measured at 2.08 and 1.97 eV for K^+ salt and 2.32 and 2.10 eV for Rb^+ salt, respectively. The energy gaps are consistent with a dark orange/dark red color for K^+ salt and an orange/dark orange color for Rb^+ salt, respectively. A red shift in absorption edge in the glassy phases is a common phenomenon as glass formation generally induces substantial defects and mid-gap states to give a lower band gap than the crystalline counterpart.[21] This creates optical contrast and can be a useful feature for optical storage systems based on phase-change materials.[22]

The results of Raman spectroscopy and PDF analysis (see below) shed light on the local structure in the glass and how these materials can readily recover their crystal structure from the amorphous state. The Raman spectrum of crystalline $K_2P_2Se_6$ at room temperature shows shifts at 154(bw), 221(s), 236(m), 259(m), 388(w), 496(w), and 514(vw) cm^{-1}, Figure 8. The shift at 221 cm^{-1} is unambiguously assigned to the P_2Se_6 stretching mode by comparison in the A_g stretching mode of

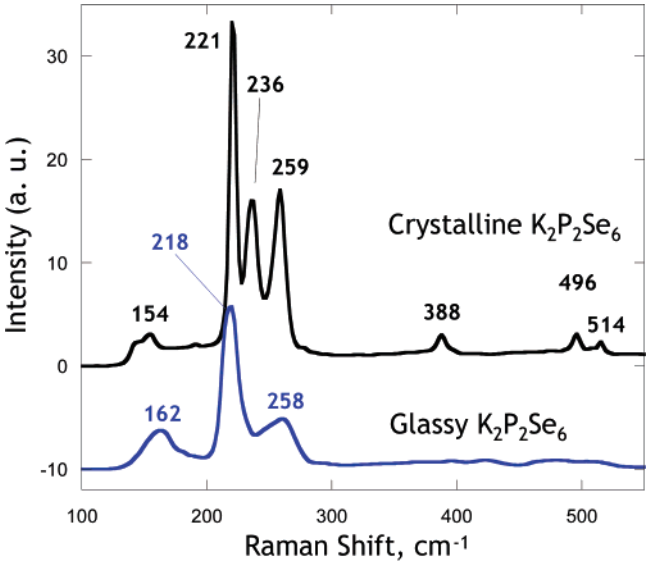

Figure 8. Raman spectra of crystalline (black line) and glassy (blue line) $K_2P_2Se_6$ at room temperature. The similar but broader features in the spectrum of the glass suggest the local structure is preserved but long range order is lost.

D_{3d} symmetry of $[P_2Se_6]^{4-}$ ligand.[23] Other peaks at 154, 496, and 514 cm^{-1} are also related with the P_2Se_6 fragment.[24] By analogy, shifts at 236 and 259 cm^{-1} can be assigned to antisymmetric and symmetric Se−Se stretching vibration modes of the diselenide group, respectively.[25]

The Raman spectrum of glassy $K_2P_2Se_6$ shows that broader and weaker peaks at 162 (bw), 218 (bm), and 258 (bw) are observed, whereas the overall peak pattern is similar to that of the crystals. This suggests that the $[P_2Se_6]$ unit and Se−Se bonds are still intact and the local structural motifs are largely preserved in the glass but crystallographic long-range order is lost. This situation makes it easy to restore the crystal structure from the amorphous state for the reversible crystal-glass phase transition.

To probe the local structure of both the glassy and crystalline forms of $K_2P_2Se_6$ we performed a pair distribution function (PDF) analysis. This technique is emerging as a useful tool for the analysis of the local structure of crystalline and noncrystalline compounds.[26] The PDFs are shown in Figure 9. Also shown in blue is the calculated PDF based on the room-temperature single-crystal structure model of $K_2P_2Se_6$. There appears to be good agreement between the crystal structure model and the experimentally determined PDF of $K_2P_2Se_6$. This in fact validates the correctness of the crystal structure.

The PDF of the glass shows well-defined correlations up to ~8 Å with the first two at 2.2 and 3.6 Å being very similar to those of the crystalline form. The interatomic correlations in the structure disappear above ~8 Å indicating the lack of long range order periodicity. The first strong correlation at 2.2 Å is assigned to Se−Se, P−Se, and P−P bonds in the structure. The second strong peak at 3.6 Å is assigned to K···Se and second neighbor Se···Se distances. The PDF data suggest that the crystalline and glassy forms of $K_2P_2Se_6$ are structurally similar which implies that the $[P_2Se_6]$ units remain intact in the glass form. This is also in agreement with the Raman spectroscopic data discussed above. The close structural relationship between crystal and glass, coupled with the stoichiometric nature of the composition, accounts for the facile congruent crystallization

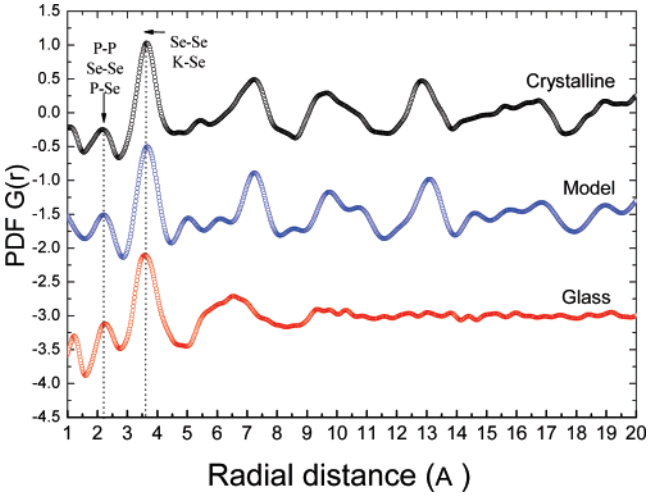

Figure 9. Pair distribution function $G(r)$ of the crystalline and glassy $K_2P_2Se_6$.

of the glass. Similar conclusions were reached from the PDF analysis of KSb_5S_8, another interesting phase-change material, which shows that its local structure within a radius of ~5 Å in the glass phase is clearly refined even though long range order is not observed.[20]

3.5. Infrared Transmission and Nonlinear Optical Properties. Materials with large NLO susceptibilities for IR application are highly sought. $AgGaQ_2$ (Q = S, Se), $ZnGeP_2$, and GaSe are main infrared materials,[27] and we recently introduced the promising long wave IR NLO compound β-$K_2Hg_3Ge_2S_8$.[28] The chalcophosphates are an attractive class in which to search for new NLO materials in that basic building units of $[PQ_4]^{3-}$ or $[P_2Q_6]^{4-}$ frequently form noncentrosymmetric arrangements by coordination to central metals or polychalcogenide fragments $[Q_n]^{2-}$. Examples include $APSe_6$ (A = K, Rb),[6] $ANb_2P_2S_{12}$ (A = K, Rb, Cs),[15] $A_{11}U_7(PS_4)_{13}$ (A = K, Rb),[16] $Cs_2CuP_3S_9$,[20] $Na_{0.5}Pb_{1.75}PS_4$,[30] and $A_3AuP_2Se_8$ (A = K, Rb, Cs).[31] In addition, chalcogenide compounds demonstrate better polarizability than oxide compounds, which have been predominantly studied for NLO application and wide IR transmission.

$K_2P_2Se_6$ exhibits wide optical transparency ranging from long wave IR (LWIR) to near-IR (NIR)/visible light, Figure 10. The mid-IR transmittance spectrum showed little absorption from 505 cm^{-1} (19.8 μm) to 4000 cm^{-1} (2 μm). There is no light absorption below the band gap transition suggesting uninterrupted light transmission in the compound. The optical transparency extends over to its absorption edge of 2.08 eV (596 nm) in the visible region. Above 19.8 μm in the far-IR region, the compound exhibited a complex set of absorptions, consistent with its Raman and far-IR spectra. Optical transparency is a key feature for materials aimed at NLO applications. For example, the important NLO material for IR applications, $AgGaSe_2$,[27] shows an LWIR transmission up to 17 μm.

The polar, noncentrosymmetric helical chain structure of $^1_\infty[P_2Se_6^{2-}]$ composed of easily polarizable P and Se atoms linked by covalent bonding can produce large optical nonlinearity. SHG measurements were performed using a modified Kurtz powder method[32] with an IR light source ranging from 1000 to 2000 nm. SHG intensities of crystalline $K_2P_2Se_6$ were directly compared with that of $AgGaSe_2$ powder. All samples were prepared in a similar fashion, and the same particle size

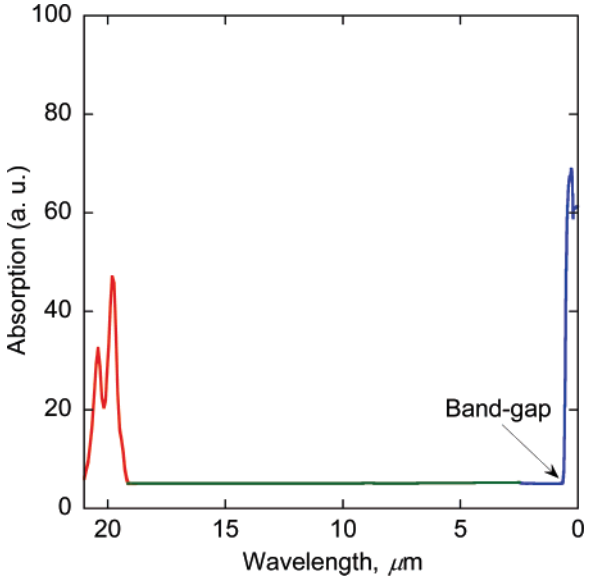

Figure 10. Far-IR (red line)/mid-IR (green line)/vis (blue line) absorption spectra of crystalline $K_2P_2Se_6$. Wide transparent range of crystalline $K_2P_2Se_6$ above the absorption band at 19.8 μm at far-IR region through mid-IR to 0.596 μm at visible region is shown.

range of 45.5 ± 7.5 μm was measured and compared. Crystalline $K_2P_2Se_6$ generated strong double frequency signals from the fundamental idler beam. The SHG intensity of $K_2P_2Se_6$ showed a maximum at 789 nm which is ~50 times larger than that at the same wavelength. Under the same experimental conditions $AgGaSe_2$ showed an SHG maximum at 890 nm, and at this wavelength the corresponding response of $K_2P_2Se_6$ was 20-fold higher. At shorter wavelengths the $K_2P_2Se_6$ outperforms the chalcopyrite material by over 100-fold, Figure 11a. These results demonstrate that the crystalline $K_2P_2Se_6$ is very promising in IR NLO applications. For comparison, the absolute nonlinear optical susceptibility at 2.12 μm of $AgGaSe_2$ and $LiNbO_3$ is 67.7 ± 13 and 29.1 ± 5.2 pm/V, respectively.[33]

The SHG intensity of the crystalline phase increased with the particle size and reached a plateau, Figure 11b. In principle, phase-matchable samples reach maximum intensity, and then for larger average particle sizes the intensity is size-independent because of the existence of a phase-matching direction in the sample.[32] In this regard, crystalline $K_2P_2Se_6$ is type I phase-matchable and eminently suitable for consideration in applications.

These results suggest that $K_2P_2Se_6$ is of special interest for the middle and deep infrared (IR) applications due to its large nonlinear optical coefficients and high transmission in the IR region. The phase matching and transmission characteristics of $K_2P_2Se_6$ should allow 3-wave interactions in the mid- and near-IR, particularly for optical parametric oscillator (OPO) devices pumped with a Nd:YAG laser, a frequency mixing of OPO outputs pumped by a Ti:Sapphire or Nd:YAG laser, as well as frequency mixing Nd:YAG laser with dye and Ti:Sapphire or other laser sources. $K_2P_2Se_6$ is also promising as an efficient frequency doubling crystal for infrared radiation such as 10.6 μm output of CO_2 lasers.

3.6. Second Harmonic Generation Response of Glassy $K_2P_2Se_6$. Surprisingly, the glassy $K_2P_2Se_6$ powder exhibited an SHG response, and its intensity is 38% that of $AgGaSe_2$.

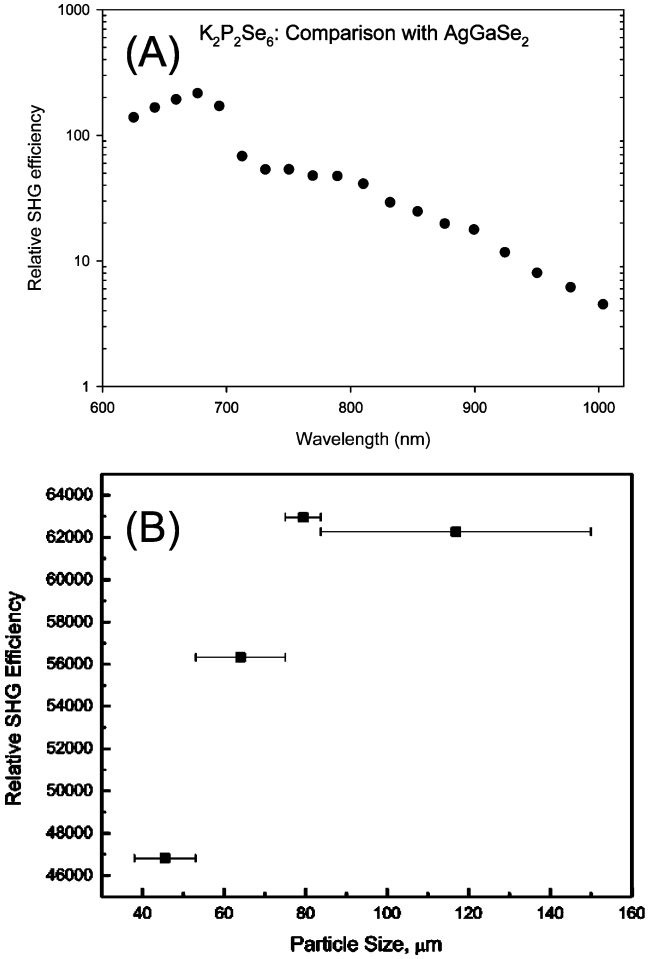

Figure 11. (a) SHG response of $K_2P_2Se_6$ relative to $AgGaSe_2$ over a wide range of wavelengths. (b) Particle size to SHG intensities diagram of crystalline $K_2P_2Se_6$ showing type-I phase-matching.

Because of great optical transparency and potential formability, there have been tremendous efforts to induce SHG in glasses[34] for use in optical fibers in telecommunications. The observation of significant NLO activity in $K_2P_2Se_6$ glass could be a rare example of this property found in an amorphous material with no specific treatment such as thermal poling, electron beam irradiation, and so on.[35] Since $K_2P_2Se_6$ is a phase-change material and retains its local structural motif in the glassy phase, we expect the noncentrosymmetric arrangement to be partially preserved and consequently to exhibit some SHG response. Indeed, the SHG response of the $K_2P_2Se_6$ glass started to be observed at a longer wavelength than that of the crystal. This suggests that the SHG signal was generated from the glass the band gap of which is red-shifted relative to the crystal, and probably did not originate from traces of the recrystallized phase embedded in the glass matrix. X-ray powder diffraction patterns after the SHG measurements did not show evidence of crystallization. It cannot be completely ruled out, however, that idler beam-induced crystallization of glass may be occurring. Additional work will be necessary to better understand the NLO properties of the glass.

3.7. Thermal Properties of $K_2P_2Se_6$. The thermal properties, such as thermal expansion, are important properties relevant to crystal growing for NLO applications. The thermal expansion of $K_2P_2Se_6$ crystal was determined by a single-crystal X-ray

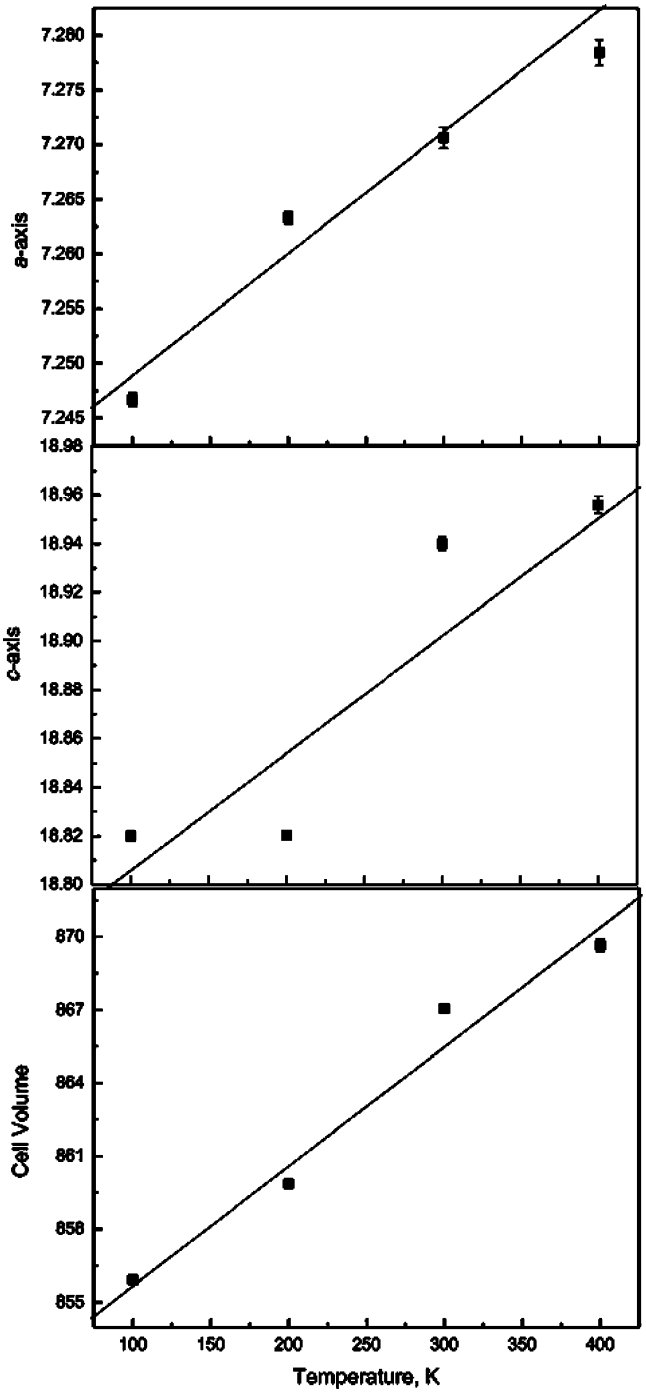

Figure 12. Temperature variation of the lattice parameters and cell volume for $K_2P_2Se_6$ from 100 to 400 K.

diffraction study in the range of 100−400 K, Figure 12. The linear (eq 2) and thermal expansion coefficients (eq 3) are defined as

$$\alpha_t = \frac{1}{L_t}\frac{dL_t}{dT} \quad (2)$$

and

$$\beta = \frac{1}{V}\frac{dV}{dT} \quad (3)$$

where L_t is the unit cell dimension along t-axis and V is the unit cell volume. Because $K_2P_2Se_6$ exhibited $2a \times 2b \times c$ supercell, the a-axis distance was divided by 2 for the calculation. The thermal expansion coefficients of $K_2P_2Se_6$ were calculated to be $\alpha_a = 1.46 \times 10^{-5}$/K and $\alpha_c = 2.41 \times 10^{-5}$/K, indicating somewhat isotropic expansion. For comparison, corresponding values for other relevant infrared NLO materials are provided: $AgGaSe_2$ ($\alpha_{\|c} = -0.81 \times 10^{-5}$/K, $\alpha_{\perp c} = 1.98 \times 10^{-5}$/K, 298−423 K),[36] $AgGaS_2$ ($\alpha_{\|c} = -1.32 \times 10^{-5}$/K, $\alpha_{\perp c} = 1.27 \times 10^{-5}$/K, 298−523 K),[37] and $ZnGeP_2$ ($\alpha_{\|c} = 1.59 \times 10^{-5}$/K, $\alpha_{\perp c} = 1.75 \times 10^{-5}$/K, 293−573 K).[38] The α of stainless steel is 1.73×10^{-5}/K at 293 K. Most importantly, $K_2P_2Se_6$ does not exhibit the anomalous behavior of $AgGaQ_2$ (Q = S, Se) which contracts along the a- and b-axes and expands along the c-direction. The latter is an anomaly which can cause thermomechanical stress in high-power applications and failure.[39]

The volumetric thermal expansion coefficient of $K_2P_2Se_6$ at $\beta = 5.35 \times 10^{-5}$/K also indicates its moderate thermal expansion. It is noteworthy that crystals of $K_2P_2Se_6$ did not show any signs of cracking or deformation when exposed to abrupt temperature change (200 K/h) or soaked at a high temperature of 500 K for several days.

4. Concluding Remarks

The compounds $A_2P_2Se_6$ (A = K, Rb) have novel chiral structures composed of helices of $^1_\infty[P_2Se_6^{2-}]$. The chirality combined with its phase-change behavior could enable $A_2P_2Se_6$ to be explored as a multifunctional switchable material. On cooling $K_2P_2Se_6$ is susceptible to a displacive phase transition to a lower space group that seems to be driven by the coordination sphere expansion of the alkali ions. If correct, the phase transition could also be effected by the application of high pressure as a means of achieving coordination sphere expansion. When molten the compounds can be quenched to a glassy state and exhibit reversible crystal-glass phase change behavior. The optical absorption edge for the glassy phase is red-shifted, and on the basis of Raman spectroscopy and PDF analysis it appears that the main building motifs are largely intact in the glassy form. This accounts for the facile restoration of the crystal structure from the corresponding amorphous phase.

$A_2P_2Se_6$ (A = K, Rb) and the previously described $APSe_6$ (A = K, Rb, Cs) are the only reported extended structure compounds in the alkali chalcophosphate family to exhibit easy glass-formation and phase-change properties. This suggests that polymeric chalcophosphates have broad glass-forming tendencies and may constitute a fertile source for stoichiometric chalcogenide glasses. The glass forming property of these materials makes them potentially valuable for producing IR optical glass fibers. Finally, $K_2P_2Se_6$ widely transparent in the mid-IR up to 19.2 μm that is coupled with a very large SHG response. The material is type-I phase-matchable with a response that is over 50 times larger than that of top performing NLO material $AgGaSe_2$. The remarkably stronger response is attributed to the helical structure of the selenophosphate which is highly polar, in contrast to the weakly polar chalcopyrite structure of $AgGaSe_2$. This makes $K_2P_2Se_6$ one of the best NLO materials known for nonresonant SHG. Finally, the glassy form of $K_2P_2Se_6$ exhibited a surprising SHG response with no poling treatment.

Acknowledgment. Financial support from the National Science Foundation (Grant DMR-0702911) and the National Science Foundation under US/Ireland cooperation (Grant 0306731) and the Northwestern Materials Research Center under the NSF (Grant DMR-0520513) for J.I.J. are gratefully acknowledged.

Supporting Information Available: X-ray crystallographic file (in CIF format) as well as tables for structural information. This material is avalable free of charge via the Internet at http://pubs.acs.org.

JA075096C